International Journal of Heat and Mass Transfer 107 (2017) 956–971

Contents lists available at ScienceDirect

International Journal of Heat and Mass Transfer

journal homepage: www.elsevier.com/locate/ijhmt

Numerical simulation of conjugate heat transfer and surface radiative heat transfer using the P_1 thermal radiation model: Parametric study in benchmark cases.

Carlo Cintolesi [a,*], Håkan Nilsson [b], Andrea Petronio [c], Vincenzo Armenio [a]

[a] University of Trieste, Dipartimento di Ingegneria e Architettura, Piazzale Europa 1, I-34127 Trieste, Italy
[b] Chalmers University of Technology, Department of Applied Mechanics, SE-412 96 Göteborg, Sweden
[c] IEFLUIDS S.r.l., Piazzale Europa 1, I-34127 Trieste, Italy

ARTICLE INFO

Article history:
Received 7 September 2016
Received in revised form 1 November 2016
Accepted 1 November 2016
Available online 8 November 2016

Keywords:
Thermal radiation
Surface radiative heat transfer
Conjugate heat transfer
P_1-model
Thermal coupling

ABSTRACT

A parametric investigation of radiative heat transfer is carried out, including the effects of conjugate heat transfer between fluid and solid media. The thermal radiation is simulated using the P_1-model. The numerical model and the thermal coupling strategy, suitable for a transient solver, is described. Such numerical coupling requires that the radiative equation is solved several times at each iteration; hence, the computational cost of the radiative model is a crucial issue. The P_1-model is adopted because of its particularly fast computation. First, a collection of benchmark cases is presented and used to carefully validate the radiation model against literature results and to analyse the model prediction limits. Despite the simplicity of the model, it satisfactorily reproduces the thermal radiation effects. Some lack of accuracy is identified in particular cases. Second, a number of benchmark cases are described and adopted to investigate fluid–solid thermal interaction in the presence of radiation. Three cases are designed, to couple radiation with: pure conduction, conduction and forced convection, conduction and natural convection. In all the cases, the surface radiative heat transfer strongly influences the system thermodynamics, leading to a significant increase of the fluid–solid interface temperature. The main non-dimensional numbers, related to the mutual influence of the different heat transfer modes, are introduced and employed in the analyses. A new conduction-radiation parameter is derived in order to study the conductive boundary layer in absence of convective heat transfer.

1. Introduction

In thermal and combustion engineering, the radiative heat transfer (RHT) strongly influences the overall heat transfer; therefore the radiative effects cannot be neglected in accurate analyses of many practical and industrial applications. This is especially true for high-temperature systems, like combustion devices (engines, rocket nozzles, furnaces), solar collectors and nuclear reaction in power plants. Yet, radiation can influence low-temperature systems, leading to non-negligible effects when combined with convection and conduction (electric ovens, lamp bulb enclosures, room heating systems).

Experimental investigations of the above-mentioned problems can be expensive and laborious. It is therefore of interest to develop and validate accurate and fast-response numerical simulation methods for studying such thermo-fluid dynamics systems. Accurate simulations of thermal radiation effects pose big challenges:

(i) from a physical point of view, radiation is a remarkably complex phenomenon. A mathematical model for RHT can be only derived under simplified hypotheses;
(ii) particular attention must be paid to the interaction with fluid medium. An effective coupling strategy has to be adopted, especially in the presence of buoyancy driven flow or participating medium (*i.e.* a medium that absorbs, emits or scatters radiation);
(iii) heat exchange at a fluid–solid interface often plays a crucial role. The surface heat transfer by conduction and radiation are strongly coupled between each other and a suitable conjugate heat transfer (CHT) strategy needs to be adopted.

* Corresponding author.
E-mail addresses: carlo.cintolesi@gmail.com (C. Cintolesi), hakan.nilsson@chalmers.se (H. Nilsson), a.petronio@iefluids.com (A. Petronio), armenio@dica.units.it (V. Armenio).

http://dx.doi.org/10.1016/j.ijheatmasstransfer.2016.11.006
0017-9310/

A thermo-fluid dynamic numerical solver, that takes in consideration all these aspects, is here described and tested in several benchmark cases. To the best of the authors knowledge, this is the first time that an extensive study of the interaction between thermal radiation and conjugate heat transfer is presented.

The general theory of thermal radiation has been extensively studied in the last century. A comprehensive theoretical background on this subject is presented by Modest [23] and Howell et al. [17]. They describe the physics of thermal radiation and derive the RHT equation. They also address the engineering treatment of thermal radiation, with a description of a number of approximation methods that are generally used. Other milestones in the field are the book of Viskanta [35], that deals with radiation in combustion systems, and the work of Hottel and Sarofim [15], that (albeit quite outdated) collects a large number of details about physical measurements of radiative quantities. A number of approximation methods for RHT, each one valid only under specific assumptions, have been proposed. We refer to Viskanta [36], Viskanta and Mengüç [37] for a detailed review of such general methods, and to Carvalho and Farias [3] for an overview on numerical models for combustion systems.

Nowadays, the most popular numerical solution approaches for RHT in participating media, are subdivided into the following families: discrete ordinates methods (DOM), spherical approximation (P_N) methods and Monte Carlo methods (MCM). The RHT equation is an integro-differential equation that depends on the direction of the radiation propagation. In the DOM approach, the equation is discretised along a finite number of directions, and the integral term is approximated by numerical quadrature. It can lead to very accurate results, but its accuracy strongly depends on the quadrature scheme used. Moreover, a correct resolution requires a fine angular and spatial discretisation; thus, it is highly computational demanding (see Hassanzadeh and Raithby [14], Modest [23]). The general strategy of the P_N approach is to expand the radiative functions in series of spherical harmonics, and to use their orthogonality properties over a sphere to convert the RHT equation to a relatively simple partial differential equation. Compared to the DOM, this method is computationally cheaper but it has some intrinsic drawbacks: generally speaking, it tends to overestimate the RHT and it can lose accuracy, for example, in the case of collimated irradiation or for a strongly anisotropic radiative source [23]. The MCM provides a statistical approach to the problem. For an overview on this method we refer to Howell [16] and Howell et al. [17]. The MCM is found to be accurate and requires a small computational effort. However, the non-deterministic nature of the model leads to some compatibility problems with the deterministic numerical solvers, while the stochastic noise can introduce stability issues when radiation is coupled with other processes (such as convection and conduction). Recently, also the lattice Boltzmann method has been applied to RHT problems by Asinari et al. [1] and Mishra et al. [21].

Different implementations of the aforementioned approaches give rise to a number of radiative models, that have been used in a wide range of engineering case simulations. The validation of such radiative models in fluid dynamic systems poses some problems. There are few experimental studies available for comparison purposes, and often validation has to be performed against other numerical simulation results. In this respect, two cases have been studied to a large extent: natural convection in a plain vertical channel with radiative walls [31,11,4,38,2]; buoyancy driven flow in a two-dimensional cavity with differently heated walls [12,19,24,39,40].

Concerning the fluid–solid heat transfer, we refer to Dorfman and Renner [8] for a review of the CHT techniques, while Duchaine et al. [9,10] give a detailed description and an analysis of stability and efficiency of some coupling strategies. The fluid–solid heat transfer by conduction has been studied in some archetypal cases. Among the others, Tiselj et al. [32] and Garai et al. [13] studied the effects of CHT in two-dimensional channel flow, while Cintolesi et al. [6] investigated the influence of conductive solid boundaries on the fluid dynamics of a differently heated square cavity.

To summarise, different radiation models have been developed in the past and used in numerical solvers where the solid wall is treated as a boundary condition to the fluid domain and the interaction with the solid medium is not considered. On the other hand, recently, the CHT problem has been studied by several authors, in presence of conduction and convection but neglecting radiation. Here we develop a methodology aimed at the simulation of heat transfer in solid–fluid interacting media, considering the three mechanisms, namely conduction, convection and radiation. Specifically, the first-order spherical harmonics approximation (P_1-model) for the RHT equation is adopted. It is coupled with the Neumann–Neumann CHT technique for a complete resolution of thermo-fluid dynamics problems, that involve participating fluid media and conductive solid boundaries. The numerical solver has been developed within the OpenFOAM framework. First, the numerical model and the coupling between the surface radiation and the Neumann–Neumann CHT are described. Second, the prediction capabilities and the limits of the radiative model adopted are investigated in several reference situations. Such test cases involve statistical steady-state simulations combining conduction, convection and radiation in participating media. Third, a number of new benchmark cases including conduction, convection, thermal radiation and CHT with solid walls are introduced. To the best knowledge of the authors there are no such cases available in the open literature, and they thus form a new set of benchmark cases. The cases are used in the present work for unique parametric investigations of RHT with fluid–solid surface heat transfer.

Three non-dimensional numbers describing the relative importance of the heat transfer modes in fluid medium, *i.e.* convection-conduction, radiation-convection and radiation-conduction, are derived. They are used to perform a parametric study of thermal radiation effects and to investigate the mutual interaction among the heat transfer mechanisms, together with the surface heat transfer. Notably, the heat fluxes ratio number H_f is introduced to investigate the conductive boundary layer.

The paper is organised as follows: Section 2 presents the mathematical model adopted and the numerical implementation within the OpenFOAM framework; Section 3 describes the non-dimensional numbers that govern the heat transfer modes in presence of thermal radiation; Section 4 validates the radiative model for a set of available benchmark cases without surface heat exchange; Section 5 introduces new benchmark cases for coupling of RHT and surface radiative heat exchange (SRHT), and provides a parametric study of RHT-SRHT; Section 6 gives the concluding remarks.

2. Simulation methodology

This section describes the complete thermodynamic model, including thermal radiation, conduction, convection and fluid–solid heat transfer. We limit the description to the thermodynamic solver, since it is independent of how the velocity field is solved.

The subscripts specify the particular use of a generic variable. If ϕ is the generic variable, then: ϕ_f is related to fluid region; ϕ_s is related to solid region; ϕ_w is the variable evaluated at the fluid–solid interface.

2.1. Radiative model

A detailed mathematical derivation of the P_1-model for RHT is given by Modest [23] and it is not repeated here. However, the

physical hypotheses behind the radiative model are briefly recalled: the medium is considered grey (no wavelength dependency of the emission, absorption and scattering coefficients) and diffusive (the coefficients do not depend on the direction of propagation); the enclosure surfaces are considered opaque (the rays penetrating into the body are internally absorbed) and grey diffusive (surface reflection is not taken into account).

The radiative model has to reproduce several phenomena: (i) RHT field in a participating medium; (ii) thermal radiation contribution on fluid medium temperature; (iii) SRHT at the solid conductive boundaries. A description of the mathematical model for the three above-mentioned items follows.

2.1.1. Radiative heat transfer

The governing equation and the boundary condition of the P_1-model for RHT with absorption, emission and linear anisotropic scattering from the medium read, respectively

$$\nabla^2 G(\boldsymbol{r}) = \kappa(3\kappa + 3\sigma_s - \sigma_s A)\left[G(\boldsymbol{r}) - 4\sigma T^4(\boldsymbol{r})\right] \tag{1}$$

$$\frac{\partial}{\partial \boldsymbol{n}} G(\boldsymbol{r}_w) = \epsilon \frac{3\kappa + 3\sigma_s - \sigma_s A}{2(2-\epsilon)}\left[G(\boldsymbol{r}_w) - 4\sigma T^4(\boldsymbol{r}_w)\right] \tag{2}$$

Here G is the total incident radiation function; T is the absolute temperature; $\boldsymbol{r}$ and $\boldsymbol{r}_w$ represent a point in the medium and onto the solid boundary, respectively; $\boldsymbol{n}$ is the solid boundary normal versor. Eq. (2) accounts for the radiation emitted/absorbed by the boundaries and it is known as the *Marshak's boundary condition* for the P_1-approximation. The constant coefficients are physical radiative parameters, namely: κ the total, linear absorption/emission coefficient; σ_s the total isotropic scattering coefficient; A the linear anisotropic scattering factor; ϵ the solid surface emissivity; $\sigma = 5.670 \times 10^{-8}$ W/(m^2 K^4) the Stefan–Boltzmann constant.

For comparison purposes with literature results, the radiative heat flux onto the enclosure surface is computed as

$$Q_{rad} = -\frac{1}{3\kappa + 3\sigma_s - A\sigma_s}\frac{\partial}{\partial \boldsymbol{n}} G(\boldsymbol{r}_w). \tag{3}$$

2.1.2. Radiative heat source into the fluid medium

The thermal energy evolution is governed by the convective, conductive and radiative terms. The temperature equation is

$$\frac{\partial T_f}{\partial t} + \frac{\partial u_j T_f}{\partial x_j} = \alpha_f \frac{\partial^2 T_f}{\partial x_j \partial x_j} + S_{rad}, \tag{4}$$

where u_j is the j-component of the fluid velocity field, α_f is the thermal diffusion coefficient of the medium, and S_{rad} the heat source/sink due to the presence of thermal radiation in a participating medium. The source/sink term reads

$$S_{rad}(\boldsymbol{r}) = \frac{\kappa}{(\rho C_p)_f}\left[G(\boldsymbol{r}) - 4\sigma T^4(\boldsymbol{r})\right], \tag{5}$$

where ρ is the density of the medium, and C_p is the medium heat capacity at constant pressure.

2.1.3. Radiative heat flux onto solid boundaries

Thermal radiation leads to an energy flux through the solid conductive boundaries. That flux can be converted into an explicit source/sink term S_w, to be added to the temperature equation for the solid medium, as

$$\frac{\partial T_s}{\partial t} = \alpha_s \frac{\partial^2 T_s}{\partial x_j \partial x_j} + S_w, \tag{6}$$

where S_w is non-zero only in the boundary cells, *i.e.* the solid medium cells that have at least one face at the fluid–solid interface. The source/sink term is computed as:

$$S_w = -\frac{1}{(\rho C_p)_s}\nabla \cdot \boldsymbol{q}_w, \tag{7}$$

i.e. the divergence of the thermal radiation heat flux $\boldsymbol{q}_w$ divided by the thermal inertia of the solid material. The equation for surface flux can be derived from the governing equation of the P_1-approximation [23], and it reads

$$\boldsymbol{q}_w(\boldsymbol{r}_w) = -\frac{1}{2}\left(\frac{\epsilon}{2-\epsilon}\right)\left[G(\boldsymbol{r}_w) - 4\sigma T^4(\boldsymbol{r}_w)\right]\boldsymbol{n} \tag{8}$$

on the fluid–solid interface, while it is set to be zero elsewhere.

2.2. Conjugate heat transfer

The temperature Eqs. (4) and (6) are provided with boundary conditions accounting for the fluid–solid heat transfer mechanism. The Neumann-Neumann CHT at the fluid–solid interface Γ is implemented imposing the continuity of temperature and the balance of the heat fluxes:

$$T_s|_\Gamma = T_f|_\Gamma, \tag{9}$$

$$k_s\left(\frac{\partial T_s}{\partial \boldsymbol{n}}\right) = k_f\left(\frac{\partial T_f}{\partial \boldsymbol{n}}\right), \tag{10}$$

where k is the thermal conductivity. The balance of both (9) and (10) is enforced below a prescribed tolerance. For more details on the coupling methodology herein employed, we refer to Sosnowski [29] and Sosnowski et al. [30].

We can notice that the surface radiative heat flux (8) can be directly included in the boundary condition (10), instead of being transformed in an explicit source/sink term (7) in the solid medium temperature equation. The latter approach is preferred to the former because it is found to be more numerically stable.

2.3. Numerical implementation

The numerical solver is implemented in the framework of OpenFOAM - version 2.1, an open-source toolbox written in C++. The solver performs a three-dimensional unsteady simulation of the system thermodynamics. As already mentioned, the present discussion is independent of the way in which the fluid dynamics is solved. Hence, the fluid resolution technique is not discussed here.

The new thermodynamic solver is named `coupledRadiationFoam`, and this name is used to label the results reported in the plots of the following sections. The solver is an extension of the code used by Cintolesi et al. [6], where the CHT technique was validated against experimental data for the case of natural convective flow in differently heated square cavity. The above-described P_1 radiative model has been integrated in that solver and used in the present investigation.

The code works with unstructured meshes and uses the finite volume method. Equations are discretised with a second-order central difference scheme in space, and a second-order backward difference scheme in time; thus ensuring a global accuracy of second order.

2.3.1. CHT implementation

The numerical implementation of the CHT technique, described in Section 2.2, is briefly presented; details were given by Sosnowski [29]. The heat exchange between different media is obtained through the imposition of suitable boundary conditions for temperature equations. The derivation of such conditions follows.

Consider two computational cells at the fluid–solid interface Γ. Fig. 1 sketches the boundary cells centre points (centroids) and the interface. If the temperature is stored in the centroid of the boundary cells, the discretisation of Eqs. (9) and (10) gives

$$\begin{cases} T_{Wf} = T_{Ws} \\ k_f \frac{T_f - T_{Wf}}{\Delta_f} = k_s \frac{T_{Ws} - T_s}{\Delta_s} \end{cases} \tag{11}$$

We denote $T_W = T_{Wf} = T_{Ws}$ as the value of the boundary temperature at instantaneous local thermal equilibrium. Solving the system, we obtain

$$T_W = \frac{k_f \Delta_s T_f + k_s \Delta_f T_s}{k_f \Delta_s + k_s \Delta_f}. \tag{12}$$

The Neumann condition in the fluid domain is given by

$$k_f \left(\frac{\partial T}{\partial n}\right)_{Wf} = k_s \frac{T_s - T_W}{\Delta_s}, \tag{13}$$

and an analogous condition is valid for the solid domain. When CHT is simulated, first the interface temperature (12) is calculated, then the Neumann condition (13) is explicitly set in each of the solid and fluid domains.

2.3.2. Algorithm steps

The thermodynamic solution algorithm is now briefly summarised:

1. *fluid region:* incident radiation Eqs. (1) and (2) and temperature Eq. (4) are solved for the fluid medium;
2. *thermal-radiation coupling:* the coupling between T and G is performed with a temperature-radiation sub-loop. The temperature and radiative fields are solved iteratively n times, until the coupling condition

$$\max_{cells} |T_n - T_{n-1}| < \varepsilon_0 \tag{14}$$

is globally satisfied (empirically, a tolerance $\varepsilon_0 = 10^{-6}$ is recommended);
3. *solid region:* the temperature field is solved for the solid medium;
4. *fluid–solid coupling:* the CHT loop is performed iterating steps *1–2–3* until the fluid–solid coupling conditions (9) and (10) are verified under a fixed tolerance given by

$$\max_{\Gamma-cells} |T_f - T_s| < \varepsilon_1, \tag{15}$$

$$\max_{\Gamma-cells} \left| k_f \frac{T_f - T_{Wf}}{\Delta_f} - k_s \frac{T_{Ws} - T_s}{\Delta_s} \right| < \varepsilon_2, \tag{16}$$

where the maximum is computed on the boundary cells at the interface. The values $\varepsilon_1, \varepsilon_2 = 10^{-6}$ are used.

It is found that 2–5 iterations of sub-loop *2* are sufficient to achieve thermal-radiation coupling, while 2 iterations are usually needed to reach the fluid–solid interface thermal equilibrium. A detailed description of the radiative model implementation was given by Cintolesi [5], while more details on the CHT coupling loop were given by Sosnowski [29] and Sosnowki et al. [30].

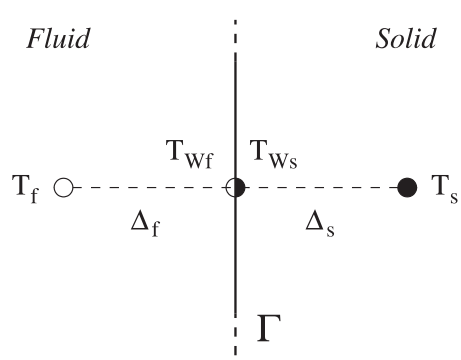

Fig. 1. Scheme for fluid–solid conjugate heat transfer computation at the interface Γ: $T_{s/f}$ is the solid/fluid temperature stored in the centroid of the boundary cell; $T_{Ws/f}$ is the solid/fluid temperature at the boundary; $\Delta_{s/f}$ is the distance between the solid/fluid centroid and the boundary.

It can be notice that for each time iteration, a number of thermal-radiation coupling loops have to be performed. Therefore, the computational power required to solve the radiative equation is multiplied by the number of loops, eventually leading to unfeasible simulations if the RHT model is highly computing demanding. The P_1-model is here adopted since it is computationally fast with respect to the other RHT models.

3. Parameters and non-dimensional numbers

3.1. Radiation

Two scaling parameters characterise RHT problems. The *linear scattering albedo*, defined as

$$\omega = \frac{\sigma_s}{\kappa + \sigma_s}, \tag{17}$$

is the ratio between the scattering coefficient and the extinction coefficient. In participating media, it represents the relative importance of scattering with respect to absorption/emission. Two scattering regimes can be identified: $\omega \sim 0$ represents either the case of high absorbing/emitting material, or of no scattering medium; $\omega \sim 1$ represents a highly scattering medium.

The *optical thickness* (or *opacity*) can be interpreted as the ability of a medium to attenuate radiation. It is defined as:

$$\tau_L = (\kappa + \sigma_s)L, \tag{18}$$

where L is the characteristic length of the medium layer. Four physical regimes of interest can be identified: non participating medium $\tau_L \sim 0$; optically thin medium $\tau_L \ll 1$, where RHT is ruled by the boundaries emission and radiation from the medium is limited; self-absorbing medium $\tau_L \sim 1$, where boundaries and internal radiation contributions balance; optical thick medium $\tau_L \gg 1$, where radiation is essentially a local phenomenon and the radiative transport behaves as a diffusion process (like molecular transport).

3.2. Heat transfer modes

A few non-dimensional numbers reflect the mutual importance of the heat transfer modes. The *Stark number*, also named *conduction-radiation parameter*, characterises the relative importance of energy transported by conduction and radiation. It reads

$$N = \frac{(\kappa + \sigma_s)k}{4\sigma \Delta T^3}, \tag{19}$$

where $\Delta T^3 = T_b^3 - T_a^3$ is the power three of the characteristic difference of temperatures of the system. The Stark number can be derived in the dimensional analysis of energy transfer equations, *e.g.* in the case of a layer of conducting-radiating medium between parallel black walls as reported by Howell et al. [17], Section 13.2.2.1 – pp. 667. Viskanta [34] gives a brief discussion on this non-dimensional number. When N decreases, radiative effects increase. Three characteristic regimes for $N = 1, 0.1, 0.01$ are usually investigated.

The non-dimensional numbers related to the other heat transfer modes can be derived as the ratio between the heat fluxes due to convection, radiation and forced conduction, that reads

$$Q_{conv} = U \rho C_p \Delta T, \tag{20}$$

$$Q_{radi} = (\kappa + \sigma_s)\sigma \Delta T^4, \tag{21}$$

$$Q_{cond} = k \Delta T / L, \tag{22}$$

respectively.

The *Boltzmann number* determines the relative importance of energy transported by radiation and forced convection, and is given by

$$Bo = \frac{Q_{conv}}{Q_{radi}} = \frac{U\rho C_p \Delta T}{(\kappa + \sigma_s)\sigma \Delta T^4}, \tag{23}$$

where U is the characteristic velocity of the flow. Venkateshan [33] gives more details on this non-dimensional number. Three regimes are investigated for $Bo = 0.1, 1, 10$, corresponding to an increasing influence of convective with respect to radiative heat transfer.

The *convection-conduction number* is the ratio between heat flux generated by forced convection and radiation, given by

$$Cn = \frac{Q_{conv}}{Q_{cond}} = \frac{U\rho C_p}{k} L, \tag{24}$$

where L is the characteristic length of the system along the direction of heat conduction. The values herein used are $Cn = 1, 10, 100$, corresponding to increasing relevance of convective heat transfer.

We can point out that analogous parameters can be derived for natural convection, substituting the expression of characteristic velocity of buoyancy driven flow $U = \sqrt{g\beta_T \Delta T L}$ into Eq. (24), where g is gravity acceleration and β_T is the thermal expansion coefficient.

Eventually, an alternative conduction-radiation is here proposed. It is derived as the ration between radiative and conductive heat fluxes within the medium, given by

$$H_f = \frac{Q_{radi}}{Q_{cond}} = \frac{(\kappa + \sigma_s)\sigma \Delta T^4}{k \Delta T} L. \tag{25}$$

Conversely to N, which includes only the physical characteristic of the participating medium, H_f takes also into account the geometrical scale of the system. The heat fluxes number H_f is found to be useful to study the convective boundary layer in Section 5.3.

3.3. Conjugate heat transfer

In transient simulations, the *characteristic diffusion time* $\mathscr{T}$ of solid materials is defined as:

$$\mathscr{T} = \frac{L^2}{\alpha_s} = \frac{(\rho C_p)_s}{k_s} L^2, \tag{26}$$

where $\alpha = k/\rho C_p$ and $\mathscr{T}$ can be interpreted as a measure of the time required to reach thermal equilibrium in solid media.

When heat transfer through the fluid–solid interface takes place, the *thermal activity ratio* (*TAR*) given by

$$TAR = \sqrt{\frac{(k\rho C_p)_f}{(k\rho C_p)_s}}, \tag{27}$$

i.e. the ratio between the thermal effusivity of fluid and solid media, can be used to quantify the interface heat flux. High values of *TAR* correspond to a weak heat flux, while small *TAR* values imply a large flux. Cintolesi et al. [6] give further details on these two parameters. We can notice that the value of the heat capacity ρC_p does not affect the final statistical steady-state configuration. Hence, in the present work, the fluid–solid thermal interaction can be characterised simply by the ratio between thermal conductivities, *i.e.*

$$R_k = \frac{k_f}{k_s}. \tag{28}$$

Lower values of R_k lead to a stronger thermal influence of the solid medium with respect to the fluid one.

4. Benchmark cases for radiative heat transfer

In this section, the SRHT and CHT are not considered, and only the fluid-medium thermodynamics is simulated. A validation of the numerical implementation is carried out, along with an investigation of the prediction capability of the P_1-model.

Two geometries sketched in Fig. 2 are used for studying a grey diffusive medium (a) between two parallel infinitely long plates, and (b) within a square enclosure. These are, respectively, one-dimensional (in a Reynolds average sense) and two-dimensional cases extensively studied in literature. Several results, both analytical and numerical are available for comparison purposes.

Different settings are used in order to investigate the following points:

- Numerical implementation is checked by comparing the numerical and the analytical solutions of the P_1-model for geometry (a), in Section 4.1;
- The pure radiative heat transfer mechanism (*i.e.* absence of conduction and convection) is investigated in both (a) and (b) geometries, for a wide number of combinations of radiative parameters, in Section 4.2;
- Combined conduction and radiation heat transfer is analysed using geometry (b), in Section 4.3.
- Combined convection, conduction and radiation heat transfer is tested in geometry (a), in Section 4.4.

The purpose is to carefully validate the radiative solver and, at the same time, to investigate the theoretical limits of the P_1-model with respect to other models proposed in literature. Table 1 reports the physical dimensions and the grid resolution used for each simulation done.

4.1. Numerical model validation

The validation of the numerical implementation is carried out for the case of an isothermal and grey medium slab, bounded by two isothermal black plates. The case geometry is sketched in Fig. 2a. The medium temperature is T_m, while the two plates are both at temperature $T_1 = T_2 = T_w$. The plates are considered black (*i.e.* the emissivity is set to $\epsilon = 1$). The participating medium can absorb/emit and scatter radiation whether isotropically or linear anisotropically.

The analytical solution of the P_1-Eqs. (1) and (2) is provided by Modest [23] (cf. chapter 16 - example 16.2 together with an exact

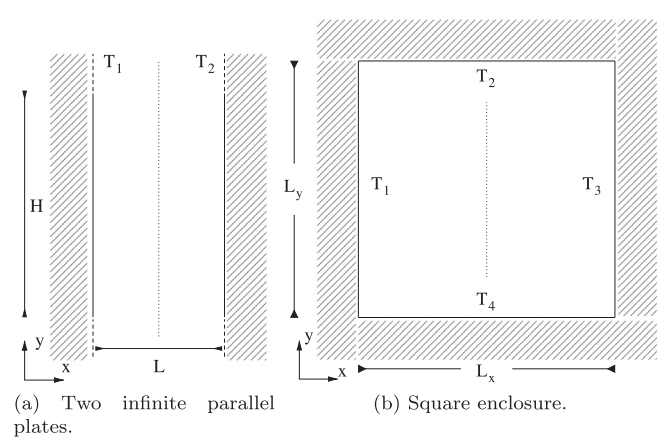

Fig. 2. Geometry of the benchmark cases for RHT validation. The presence of isothermal walls (depicted as grey regions) is reproduced by suitable boundary conditions for the fluid medium.

Table 1
Physical dimensions and computational grids for the test cases simulated in Section 4.

Section	Geometry	Dimension [m]	Grid [pts]
Section 4.1	Parallel plate	$L = 1$	31
Section 4.2.1	Parallel plate	$L = 1$	31
Section 4.2.2	Square cavity	$L_{x/y} = 1$	96×96
Section 4.3	Square cavity	$L_{x/y} = 1$	41×41
Section 4.4	Plane channel	$L = 2, H = 60$	32×960

solution of the complete RHT equations. The analytical solution is given by

$$\Psi_{ana}(\tau_x) = \frac{2\sinh\tilde{\gamma}\tau_x}{\sinh\frac{1}{2}\tilde{\gamma}\tau_L + \frac{1}{2}\sqrt{\frac{3-A\omega}{1-\omega}}\cosh\frac{1}{2}\tilde{\gamma}\tau_L}, \tag{29}$$

where $\tau_x = (\kappa + \sigma_s)x$ is the non-dimensional horizontal coordinate, also called *optical distance*, and $\tilde{\gamma} = \sqrt{(1-\omega)(3-A\omega)}$ is a scattering constant. The non-dimensional heat flux onto the plates is considered for comparison purposes, given by

$$\Psi = \frac{Q_{rad}}{\sigma(T_m^4 - T_w^4)}, \tag{30}$$

where Q_{rad} is the surface normal heat flux (3). Because of the symmetry of the problem, the origin of the axis is placed in the mid-plane between the plates; thus the plates are located at $\tau_x = \pm\tau_L/2$.

Fig. 3a shows the heat flux both for non-scattering and isotropic scattering medium, while Fig. 3b displays the case of a linear anisotropic scattering medium. In both cases, the numerical solution fits the analytical one. Since these results are obtained using a wide combination of the radiative parameters, we can conclude that the P_1-model is correctly implemented in the code.

A comparison between the exact solution and the P_1 solution highlights one of the major drawbacks of the spherical approximation method: the tendency to overestimate the thermal radiation flux. Another consideration is related to the optical thickness. In the last decade, it was alleged that the P_1-model is inaccurate in the optical thin limit, *i.e.* $\tau \to 0$. Recent investigations show that this is not a general issue [23]. In the present simulation, we can notice that P_1 goes to the correct thin limit while it loses accuracy in the thick limit.

4.2. Pure radiative heat transfer

In this section the model is validated in cases where the temperature of the medium is ruled just by thermal radiation, while convection and conduction are neglected.

4.2.1. Parallel plates

The parallel-plate geometry (Fig. 2a) is again used with other settings: the two plates are taken at different temperature $T_1 < T_2$, the scattering is neglected and the plate emissivity is set to $\epsilon = 1$. Comparisons are done against the analytical solution proposed by Howell, Siegel and Mengüç [18] for non-dimensional surface heat flux and non-dimensional temperature, respectively

$$\Psi = \frac{Q_{rad}}{\sigma(T_2^4 - T_1^4)} \quad \text{and} \quad \Phi = \frac{T^4 - T_2^4}{T_1^4 - T_2^4}. \tag{31}$$

The former is computed at the plate surfaces, the latter is plotted along a horizontal line $y = const$.

Fig. 4a reports the non-dimensional temperature distribution for several values of optical thickness of the participating medium. The results are in good agreement with the reference solutions, even if we can notice a slight discrepancy for low values of τ_L.

Fig. 4b depicts the non-dimensional heat flux for a large range of optical thickness values. The results fit the reference solutions fairly well.

Overall, the P_1-model predictions are quite accurate. The prediction of the heat flux Ψ is more precise than in the analogous case presented in Section 4.1. The lack of accuracy in the previous case can be attributed to the presence of a temperature step at the plate-medium interface. This unphysical discontinuity may affect the prediction capability of the model, and leads to less accurate results.

4.2.2. Grey medium in square enclosure

The case of a grey medium in a square enclosure is sketched in Fig. 2b. Two different radiative media are studied: (A) an absorbing/emitting, non-scattering medium and (B) a purely scattering medium. Analytical solutions are not available, but different numerical studies for these cases can be found in literature.(A) *Absorbing/emitting, non-scattering medium*: the medium has a temperature $T_m > 0$, while the enclosure walls are cold $T_{1,2,3,4} = 0$. They have constant emissivity $\epsilon = 1$. The non-dimensional heat flux on the wall,

$$\Psi = \frac{Q_{rad}}{\sigma T_m^4}, \tag{32}$$

is plotted and compared with the numerical profile of Rousse et al. [27,28]. They adopted a DOM approach, where a numerical solver based on a control volume finite element method was used to resolve the complete RHT equations. Also Crosbie and Schrenker [7] studied the same case, solving the two-dimensional governing equations. They used the modified Bessel function to obtain an integral expression of the radiative source term. The integral presented a point of singularity that was removed. Subsequently, the equations were numerically integrated with a Gaussian quadrature formula. The data obtained in the latter work are in perfect agreement with those of the former, hence they are not explicitly reported.

Fig. 5 shows the heat flux at the bottom wall of the cavity, for three increasing values of optical thickness. The results become more and more inaccurate as the optical thickness of the medium increases. Specifically, the P_1-model fails to reproduce Ψ in the proximity of the vertical walls, where the increase of heat flux is underestimated.

The lack of accuracy for large values of τ_L is expected, since it is known that the P_1-model is not suitable for optical thick media [23]. An explanation for the behaviour in the proximity of the vertical wall is provided hereafter: the P_1-equation provided with the Marshak's boundary condition is not accurate when the wall emission strongly affects the thermal radiation, *i.e.* the effects of the participating medium are limited. In the cavity corner region ($x/L_x < 0.1$) the radiative effects of the vertical and horizontal cold walls combine, leading to a decrease of temperature and to a less accurate prediction than in the central region ($0.1 < x/L_x < 0.9$). Moreover, the corner region can be affected by *collimate radiation* (thermal rays impinge the solid surfaces in a almost tangential direction), that is difficult to reproduce by the spherical approximation models [23].

(B) *Purely scattering medium*: the enclosure walls are cold $T_{1,2,3} = 0$, except for the bottom one at $T_4 > 0$. Several cases are simulated, changing the wall emissivity ϵ and the optical thickness τ_L. The non-dimensional surface heat flux,

$$\Psi = \frac{Q_{rad}}{\sigma T_4^4}, \tag{33}$$

is compared with the results reported by Rousse et al. [28] and Modest [22], who uses a differential approximation to solve the radiative equation.

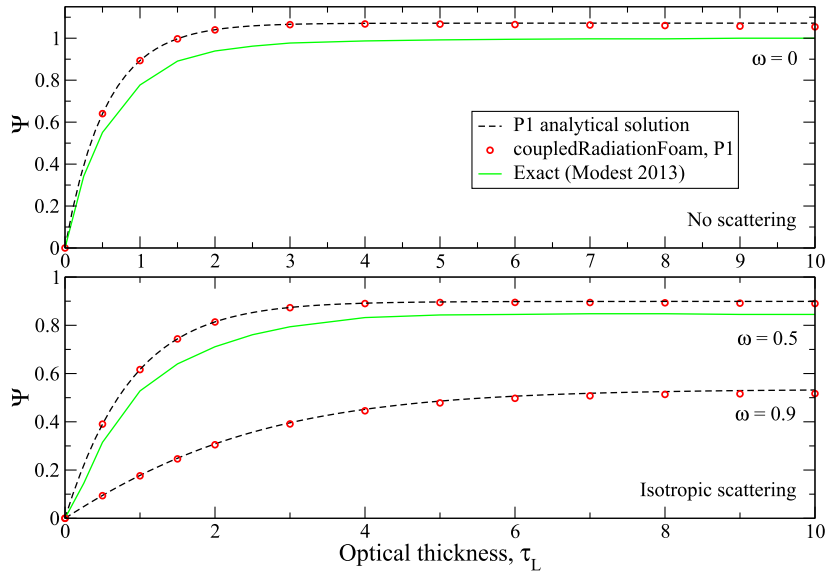

(a) Test without linear isotropic scattering, $A = 0$.

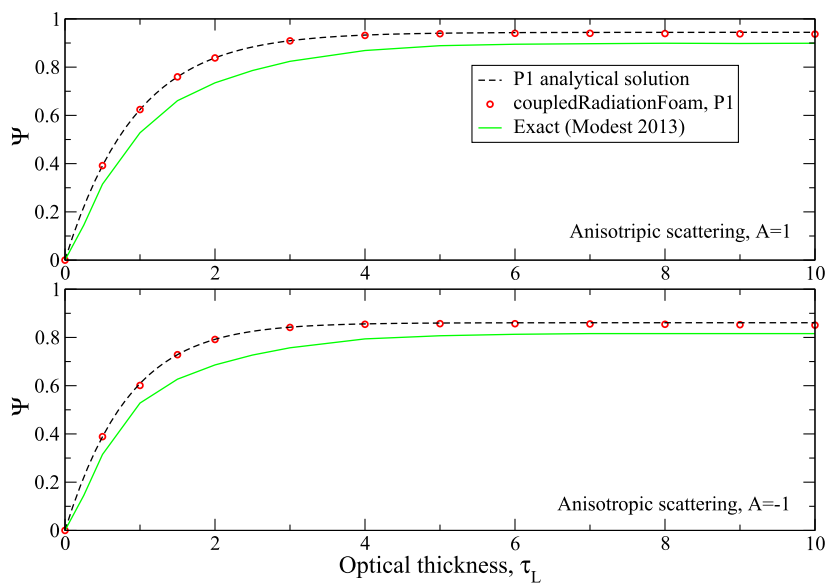

(b) Test with linear scattering $\omega = 0.5$ and two values of linear isotropic scattering A.

Fig. 3. Isothermal grey solid medium between two parallel walls. Labels: dash line, analytical solution of P_1-equation [23]; red circle, numerical solution of P_1-equation; green line, exact solution of the RHT equation [23]. (For interpretation of the references to colour in this figure caption, the reader is referred to the web version of this article.)

Fig. 6a depicts the effects of the optical thickness on the heat flux, at the bottom hot wall. Several simulations are performed, setting the wall emissivity to $\epsilon = 1$ and increasing the optical thickness τ_L. Surprisingly, the results become more accurate for optical thick media. Similar to the previous simulation (A), the P_1-model fails in the corner region.

In order to better understand the impact of the boundaries on the overall thermal radiation, the same simulations are re-run using several decreasing values of the enclosure wall emissivity. Empirically, the value $\epsilon = 0.6$ allows a perfect reproduction for $\tau_L = 1$ and improves the prediction for the other cases. The profiles are reported with a dash blue line in Fig. 6a. This test corroborates the fact that the Marshak's condition for the P_1-model does not reproduce correctly the walls radiation contribution: it tends to amplify the wall influence in the global radiation. Hence, this is the main source of error in those cases when wall radiation mainly rules the total radiation. Unfortunatly, the Marshak's boundary condition is the only one available for the P_1-model at the moment (Ref. Modest [23]). In the last years, efforts have been devoted to improve the formulation of Marshak's condition for the P_1-model. Among the others, we refer to the work of Liu et al. [20], that has introduced a corrective parameter to obtain better predictions.

Fig. 6b shows the effect of varying the wall emissivity, when the optical thickness is set to $\tau_L = 1$. Overall, the results are largely overestimated. When the wall emissivity decreases and the effects

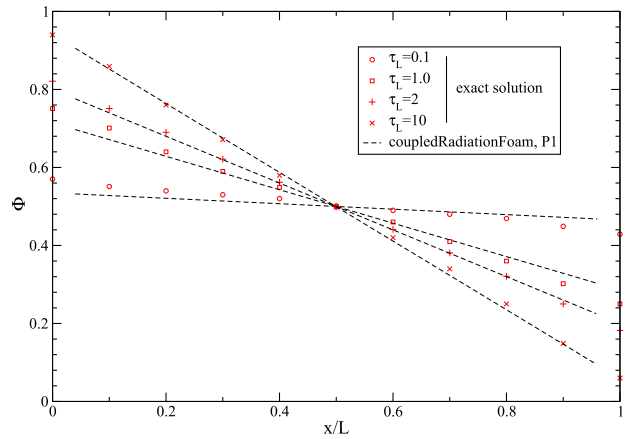

(a) Temperature distribution between the two plates for different optical thickness of the medium.

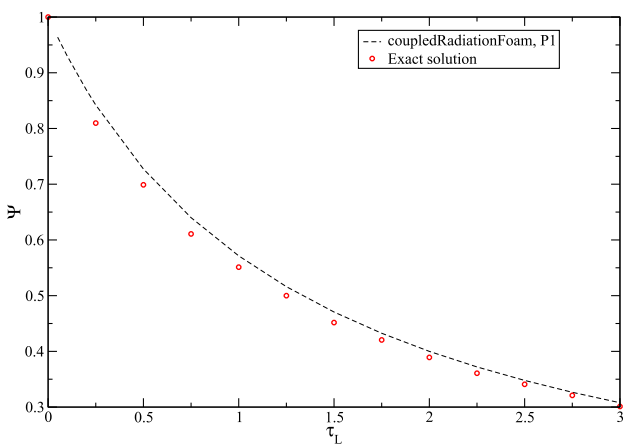

(b) Heat flux on the plates with respect to the optical thickness of the medium.

Fig. 4. Isothermal grey solid medium between two parallel walls. Comparison between the P_1-model and the exact solution [18].

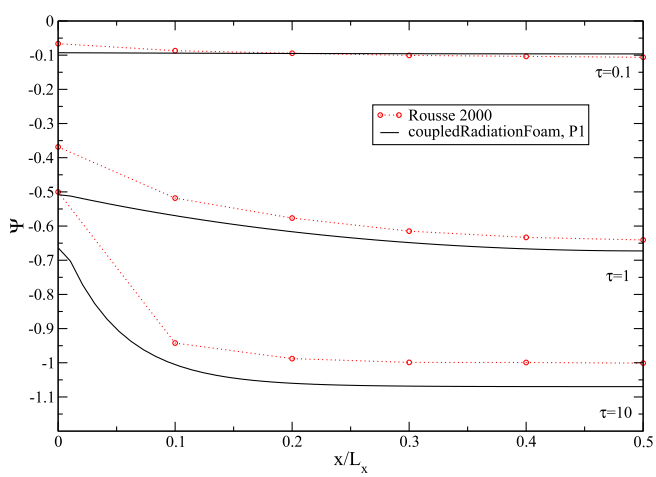

Fig. 5. Non-dimensional heat flux on the bottom wall of the square enclosure. Labels: red circles, data from Rousse et al. [28]; black line, P_1-model solution. (For interpretation of the references to colour in this figure caption, the reader is referred to the web version of this article.)

of the boundaries are less intense, the predictions are more accurate. The relative error is also computed using the formula $e_{rel} = (\Psi - \Psi_{ref})/\Psi_{ref}$, where Ψ_{ref} are the reference data [28]. For

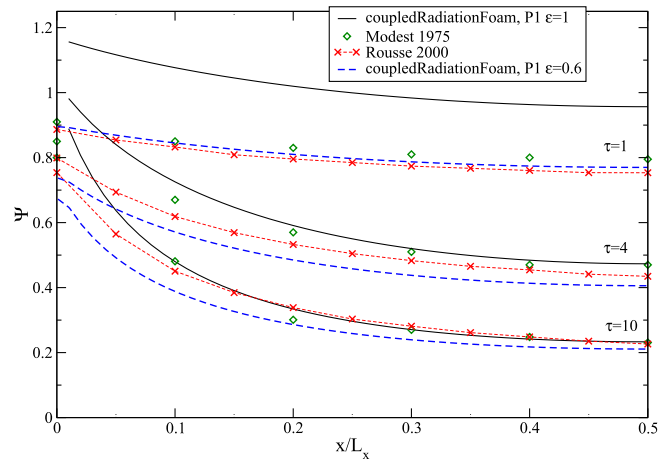

(a) Effects of the variation of wall emissivity ϵ.

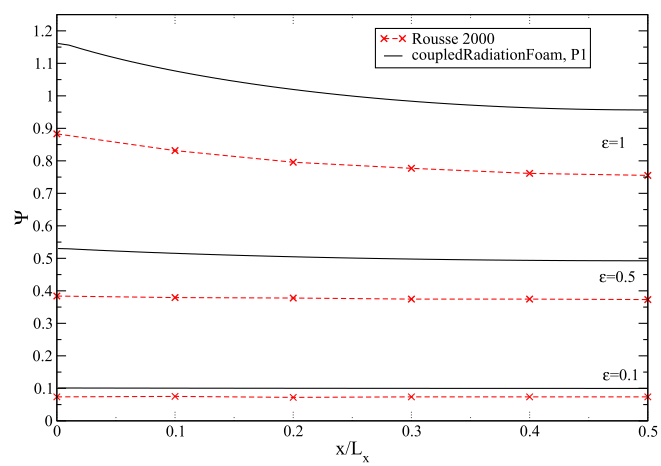

(b) Effects of the variation of optical thickness τ_L.

Fig. 6. Non-dimensional heat flux on the bottom wall of the square enclosure. Labels: red cross, data from Rousse et al. [28]; green diamonds; data from Modest [22]; solid and dash line, P_1-model solution. (For interpretation of the references to colour in this figure caption, the reader is referred to the web version of this article.)

all the cases the relative error is almost constant along the x/L_x direction and spans in the range $0.3 < e_{rel} < 0.4$.

In conclusion, we can note that the case of pure scattering (B) exhibits results worse than the case of pure absorbing/emitting medium (A). *A priori*, this is not expected because the contribution of the scattering on the governing equations (1) and (2) is analogous to the absorbing/emitting contribution. The only difference in the use of the σ_s and κ, is that the absorption coefficient multiplies the entire right hand side of the incident radiation equation. If $\kappa = 0$ the radiation equation would reduce to a Laplace equation, and G would be completely determined by the boundary conditions. This is not happening when $\sigma_s = 0$. Therefore, it is not the presence of scattering that introduces an error, but the absence of the absorption/emission that amplify the influence of the boundaries emission (ruled by Marshak's condition) and eventually entails a lack of accuracy.

4.3. Combined conduction and radiation

RHT is here activated together with heat conduction. The case geometry studied is the square cavity depicted in Fig. 2b. The bottom wall has a constant temperature $T_4 = T_w$ while the other walls have $T_{1,2,3} = T_w/2$. The medium is non-scattering, the optical

thickness is set to $\tau_L = 1$, and the walls are black ($\epsilon = 1$). The effects of conduction to radiation are ruled by the Stark number N, cf. Eq. (19).

Fig. 7 shows the non-dimensional temperature T/T_w for different values of N. The comparison is made with the numerical data of Rousse et al. [28] and Razzaque et al. [25,26], who use the finite element method to solve the RHT equation. Those two data sets practically collapse one over the other, thus only the first one is included in the comparison. A simulation of conduction without radiation is also plotted: k is determined imposing $N = 1$ and switching radiation off. This case is labelled as $N = \infty$, with an abuse of notation.

There is a quite good agreement with the reference data, although the temperature is slightly over-predicted in the proximity of the bottom wall.

4.4. Combined conduction, convection and radiation

The case studied by Viskanta [34] is here reproduced: a fully-developed laminar flow within a plain channel (Fig. 2a). The Poiseuille flow enters the channel from the bottom ($y/H = 0$) and flows out from the top ($y/H = 1$). The flow field is given by

$$u_y(x) = 6\bar{u}\left[(x/L) - (x/L)^2\right], \tag{34}$$

where the mean velocity is set to $\bar{u} = 1$. Velocity variations along the other directions are neglected. The two vertical plates are isothermal with temperature $T_1 = T_2 = T_w$, the bottom boundary is at temperature $T_{in} = 0$, while the zero gradient condition is enforced at the top boundary. The plates are black, thus $\epsilon = 1$, and the zero gradient condition is set for incident radiation G at the bottom and top boundaries. The participating medium is not scattering and the optical thickness is set to $\tau_L = 1$.

Three simulations are performed for different values of the Stark number. The non-dimensional temperature profile T/T_w is compared with the data of Viskanta [34] in Fig. 8. This author evaluated the integral–differential RHT equation with the Barbier's method, which uses a three terms Taylor expansion. The case was also studied by Rousse et al. [28], but those results are very similar to those of Viskanta [34], so they are not included in the comparisons.

Temperature is plotted over a horizontal line $y = y_0$, for which

$$T(x, y_0)|_{x/L=0.5} = T_w/2. \tag{35}$$

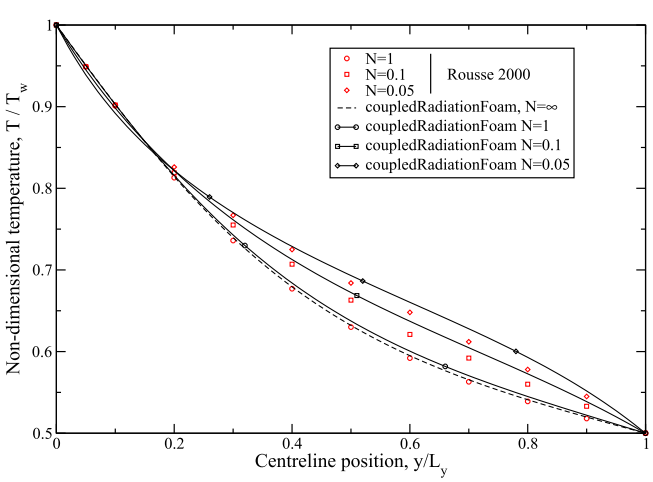

Fig. 7. Non-dimensional temperature over a vertical centreline, for conduction and radiation in a square enclosure. Simulations for different Stark number N. Labels: red symbols, data from Rousse 2000 [28]; solid lines, P_1-model; dash line, convection without radiation. (For interpretation of the references to colour in this figure caption, the reader is referred to the web version of this article.)

The location $y = y_0$ is thus different for each simulation. Particularly, when N decreases and the effects of radiation overcome conduction, y_0 is located farther from the inlet. After preliminary tests, a channel entry-length of $H/L = 7$ is found to be enough to develop the thermal profile in all cases.

The results are in good agreement with the reference values. When $N = 1$, radiation essentially does not affect the temperature. For lower values of the Stark number, temperature is not altered in the proximity of the walls but it increases in the central region. Near the wall, the temperature is still dominated by conduction because of the higher temperature gradient arising on the fluid–solid interface.

5. Surface radiative heat transfer

This section introduces and studies a benchmark case for surface heat transfer between fluid and solid media in the presence of conduction, convection and thermal radiation. To the best of our knowledge, a similar benchmark case has not been reported in the literature yet.

5.1. Geometry and general settings

Fig. 9 sketches the case geometry: it consists of two rectangular domains, with isothermal walls at the sides. The left-side region contains a fluid medium that is radiative participating. The right-side region is made of a solid material that is thermally conductive and radiative opaque. Heat transfer by conduction, forced convection and thermal radiation occurs in the fluid medium, while only heat conduction occurs in the solid medium. Surface heat transfer by contact (CHT) and radiation (SRHT) take place at the interface. This interaction leads to a strong thermal coupling between the two media.

The left isothermal wall is hot, while the right one is cold: $\Delta T = (T_h - T_c) > 0$ K. The difference of temperature is not the same for all the cases studied. It will be specified for each of the following simulations, excepted when it can be derived from the non-dimensional numbers. The solid material is a good conductor, having a higher thermal conductivity with respect to the fluid medium. The thermal conductivities ratio (28) is set to

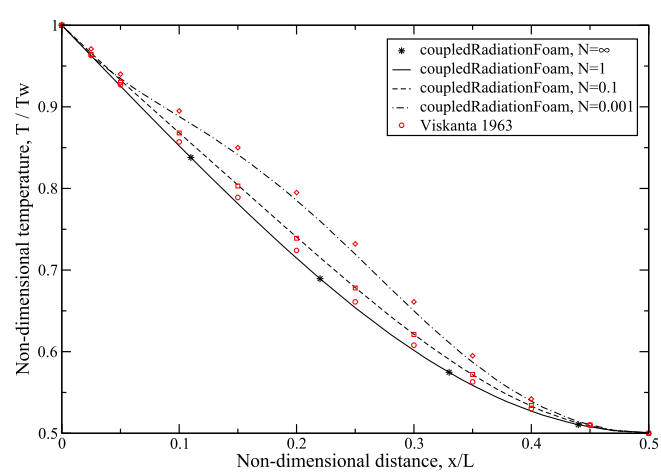

Fig. 8. Non-dimensional temperature over the horizontal line $y = y_0$ for which $T(x/L = 0.5, y_0) = T_w/2$, in case of convection, conduction and radiation in plain channel. Simulations for different Stark number N. Labels: red symbols, data from Viskanta [34]; lines, coupledHeatVapourRadiationFoam, P_1-model; black stars, coupledHeatVapourRadiationFoam without radiation. (For interpretation of the references to colour in this figure caption, the reader is referred to the web version of this article.)

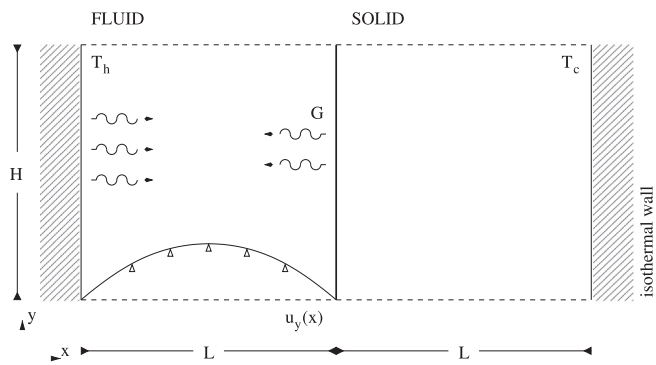

Fig. 9. Geometry of the benchmark case for SRHT.

$$R_k = \frac{1}{4}, \tag{36}$$

while the heat capacity is $(\rho C_p)_{s/f} = 10^3$ for both media. The solid boundaries of the fluid region are black ($\epsilon = 1$) and the medium is non-scattering ($\omega = 0, A = 0$), while the absorption/emission coefficient κ varies in the different cases.

5.2. Overview of simulations

The above-described system allows an investigation of the mutual influence of the three heat transfer mechanisms in the presence of a fluid–solid surface heat transfer. The thermodynamics of such a system is completely determined by the non-dimensional numbers described in Section 3.

The interaction between the following phenomena is studied:

- conduction and thermal radiation, changing the Stark number N and optical thickness τ_L, in Section 5.3;
- conduction and forced convection, varying the convection-conduction number Cn, in Section 5.4;
- conduction, forced convection and thermal radiation, for different combinations of N and the Boltzmann number Bo, in Section 5.5;
- conduction, natural convection and thermal radiation, for different values of N, in Section 5.6.

In all the cases, the participating medium is not scattering; thus $\sigma_s = 0$ and $A = 0$.

5.3. Conduction and thermal radiation

In this case the temperature is transported only by conduction and thermal radiation. Convection is not considered, hence the fluid medium is at rest, leading to a one-dimensional simulation. The width of each of the fluid and solid regions is $L = 1$ m, discretised by 80 computational points (each one). Thermal radiation propagates into the fluid medium and impinges the fluid–solid interface ($x/L = 1$), where the SRHT takes place. The radiative heat, supplied to (or subtracted from) the interface, changes the temperature distribution within the solid medium. Simultaneously, in fluid medium, the radiation field is altered by the interface temperature.

The governing parameters are the Stark number N and the optical thickness τ_L. Fig. 10 shows the non-dimensional temperature distributions:

$$\Phi = \frac{T^4 - T_c^4}{\Delta T^4}, \tag{37}$$

over a line through the fluid and solid media. Simulations have been performed for all combinations of the values $N = 1, 0.1, 0.01$ and $\tau_L = 0.1, 1, 10$. The case without thermal radiation is also simulated; it is again labelled $N = \infty$.

Fig. 10b is first analysed and used for comparison with the others. When radiation is neglected ($N = \infty$), conduction rules

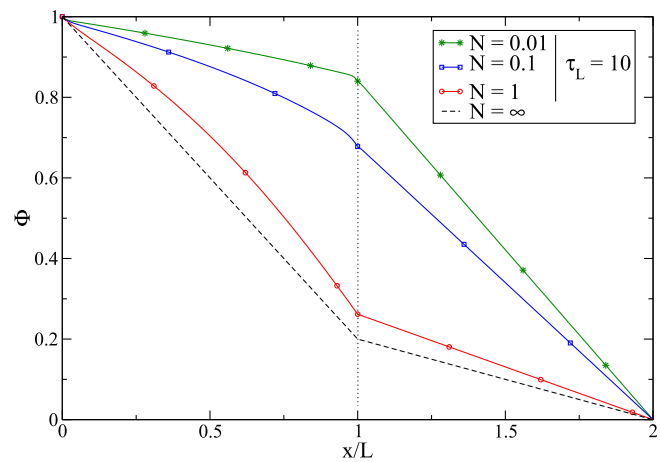

(a) Optical thick medium, $\tau = 10$.

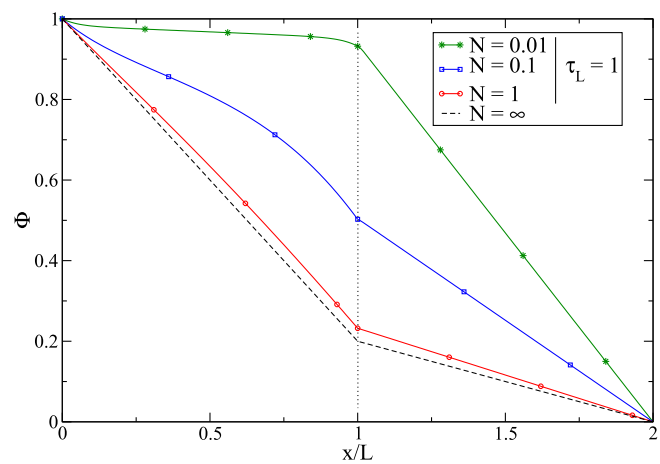

(b) Self-absorbing medium, $\tau = 1$.

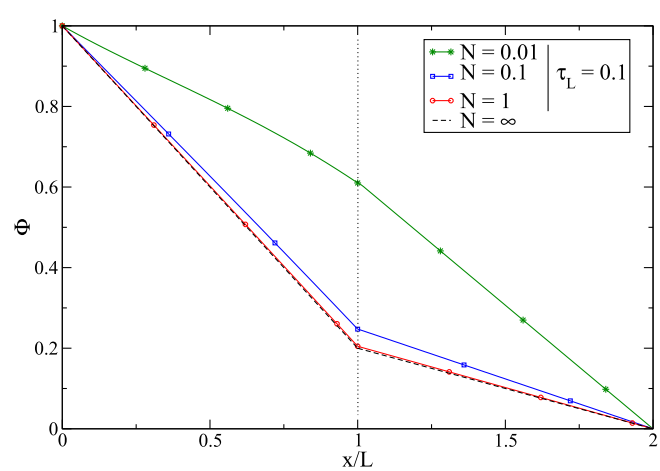

(c) Optical thin medium, $\tau = 0.1$

Fig. 10. Thermal radiation and conduction in the SRHT benchmark case. Non-dimensional temperature profile for different values of Stark number N and optical thickness τ_L.

the system and the surface temperature is one fifth of the difference of temperature between isothermal walls. This is in accordance with the thermal conductivities of the media (cf. Eq. (36)). The introduction of thermal radiation increases the overall temperature of the system. When $N = 1$, the interface is slightly heated up by the radiative effects, but the temperature distribution in the fluid medium remains linear. When $N = 0.1$, radiation significantly heats up the interface and makes the fluid temperature non-linear. Close to the solid boundaries, conduction still dominates and a quasi-linear thermal profile arises. In the fluid central zone, radiation from the boundaries and within the medium overcomes conduction and increases the temperature. The non-linear temperature distribution is expected, since thermal radiation is a phenomenon that goes like T^4. When radiation dominates ($N = 0.01$) the fluid medium is at almost the same temperature than the hot wall, and it slightly decreases when the interface is approached.

Fig. 10a depicts the thermal profiles for an optical thick medium. In the case of low and moderate radiation ($N = 1, 0.1$), the increase of the optical thickness leads to augmentation of the overall system temperature, and particularly the interface temperature. Surprisingly, for high radiation level ($N = 0.01$) the interface temperature decreases. This effect can be due to the fact that an optical thick medium acts as a barrier for radiation. The RHT process then becomes localised and behaves as a conduction process. As a matter of fact, the profile in the fluid medium is almost linear. Since the thermal conduction is weak and the energy radiated is absorbed by the fluid medium, the interface temperature decreases with respect to the case $\tau = 1$.

Fig. 10c shows the temperature profiles in the case of an optical thin medium. The fluid medium is less participative, thus the thermal radiation reaches directly the solid interface without being altered by the medium. The general effect is the reduction of the system temperature for all the cases studied. The case $N = 1$ collapses to the case $N = \infty$.

The boundary layer on which conduction overcome thermal radiation can be estimated by means of the fluxes ratio number H_f defined by Eq. (25). In analogy with the definition of optical distance form the optical thickness (see Section 4.1), we define the fluxes ratio distance as

$$H_f(x) = \frac{(\kappa + \sigma_s)\sigma\Delta T^4}{k\Delta T}x. \tag{38}$$

The energy transport is dominated by conduction when $H_f(x) \lesssim 1$ and by radiation when $H_f(x) \gtrsim 1$. The thickness of the conductive boundary layer $x_{bl}/L = \delta$ near the walls can be estimated imposing $H_f(\delta) = 1$. Table 2 reports the values of δ near the isothermal hot wall, for the nine simulations show in Fig. 10. In the optical thick case (Fig. 10a) the medium is highly participative, thus radiative heat flux is strong and the conductive layer is almost zero for all values of N. In the radiative layer the thermal profiles are non-linear. Conversely, in the optical thin case (Fig. 10c) the medium has a very weak interaction with thermal radiation; hence, the heat transfer occurs mainly by conduction and δ is larger than the total fluid region width. Consequently, the fluid temperature profiles are practically linear. In the intermediate case (Fig. 10b), the conductive layer encompasses the entire fluid region just in the case of low radiation ($N = 1$), while is quite narrow in the case of high radiation ($N = 0.01$). The case $N = 0.1$ exhibits a conductive layer comparable with the radiative one: the temperature has an almost linear behaviour within the region $\delta \lesssim 0.4$, and become non-linear in the region $\delta \gtrsim 0.4$ (before approaching the interface) where it shows a typical concave curve profile. A transition region is located in a neighbourhood of the point $\delta = 0.4$, where the thermal profile change the concavity.

Table 2
Conductive boundary layer thickness δ near the isothermal hot wall for the nine cases show in Fig. 10.

δ	$\tau = 10$	$\tau = 1$	$\tau = 0.1$
$N = 0.01$	0.0004	0.04	4
$N = 0.1$	0.004	0.4	40
$N = 1$	0.04	4	400

Fig. 11 reports the non-dimensional temperature profiles for one extra case: the wall emissivity is here changed to $\epsilon = 0.5$, while $\tau = 1$ is fixed. The decrease of the wall emissivity does not change the general behaviour of the RHT with respect to the case $\epsilon = 1$: the profiles are similar to the ones with $\epsilon = 1$, but the overall system temperature is lower and the interface temperature decreases as a consequence of the lower level of energy emitted by the hot wall.

5.4. Conduction and forced convection

This case does not involve thermal radiation. It is briefly analysed for comparison purposes with the case in Section 5.5, which includes also radiation.

The width of each regions is $L = 1$ m, while the height is chosen to be $H = 30$ m. After some preliminary simulations, this height is found to be sufficient for developing the thermal profile in all the cases simulated. The two regions are discretised using 20×600 cells, both equidistant in the y-direction and stretched in the x-direction. The fluid region grid is stretched to have a higher resolution in the thermal boundary layer. The solid region grid is stretched the same way, in order to assure the same size of the interface boundary cells in the fluid and solid regions. A double-side stretching function, based on hyperbolic tangent, is used:

$$x(\xi) = \frac{1}{2}\left(1 + \frac{\tanh(\delta_s(\xi - 1/2))}{\tanh(\delta_s/2)}\right), \tag{39}$$

where ξ are the coordinates of an equispaced partition, and the stretching factor is $\delta_s = 3.5$.

The forced Poiseuille channel flow enters from the bottom side ($y/H = 0$) and exits through the top side ($y/H = 1$). The equations of motion are not solved, but the velocity profile (34) is imposed. The value of the flow field characteristic velocity $U = \bar{u}$ changes for each simulation.

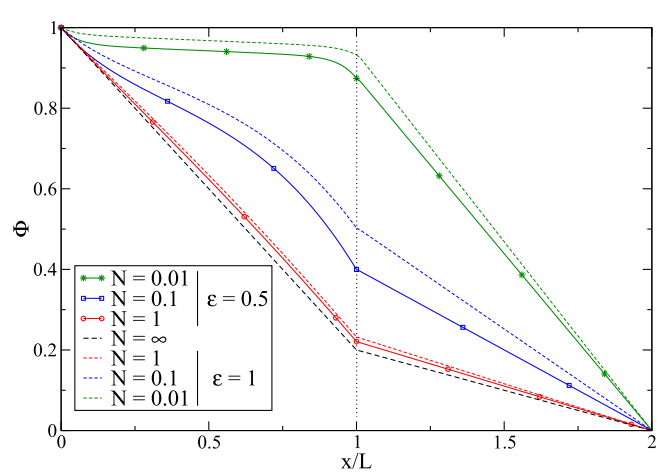

Fig. 11. Thermal radiation and conduction in the SRHT benchmark case. Non-dimensional temperature profile along a line $y = cost$ for the case of self-absorbing medium. Simulation of two values of walls emissivity ϵ, for increasing level of thermal radiation.

The temperature boundary conditions at the bottom and top sides are: for solid medium, adiabatic condition on both boundaries; for fluid medium, fixed temperature $T_{in} = 0$ at bottom, adiabatic condition at the top boundary. The adiabatic condition is imposed at the solid bottom side because our purpose is to study the effects of streamwise convection against wall-normal conduction. If a fixed temperature $T_{in} = 0$ condition, coherent with the fluid medium one, was imposed, then the conduction along the y-direction in the solid medium would affect the temperature distribution. Heat convection and conduction are here orthogonal to each other: convection cools down the fluid along the y-direction (streamwise), while conduction transports heat between the two external isothermal walls along the x-direction (wall-normal).

The fluid thermal conductivity is set to $k_f = 10\ \mathrm{W/(mK)}$ in order to have a sufficiently high characteristic diffusion time, see Eq. (26), and to quickly reach the statistical steady-state solution. This system is governed by the convection-conduction number Cn. Three simulations have been done for $Cn = 1, 10, 100$ respectively. The temperature profile is plotted along a horizontal line $y/H = Y_0$, where Y_0 satisfies:

$$T_f(x, Y_0)|_{x/L=0.5} = \frac{(T_h - T_c)}{2},$$

i.e. the height at which the temperature in the centre of the fluid region is the average between the temperature of the isothermal hot and cold walls.

The three simulations give practically the same temperature profile. In Figs. 12a,b,c we show the profile for case $Cn = 100$ as a black dash line, labelled $N = \infty$. The interface temperature is slightly lower than in the non-convective case (cf. Fig. 10, black dash line), because of the cooling effect of the fluid flow. However, convection does not strongly influence the fluid thermal profile which is almost linear. The thermal profiles remain unaltered in the three cases since the value of Y_0 increases almost linearly with Cn. Just for the case $Cn = 1$, a slight decrease of fluid medium temperature is detected. This is due to the influence of the fluid bottom temperature: when Cn is small, then Y_0 is close to the bottom and the thermal profile is affected by the heat conduction in the streamwise direction.

The influence of the bottom thermal boundary layer can be estimated by means of the conduction–convection number. The ratio between the convective and conductive heat transfer in the y-direction, at location Y_0, can be expressed as:

$$Cn(Y_0) = \frac{U\rho C_p}{k} Y_0 = Cn(L)\frac{Y_0}{L}, \tag{40}$$

following Eq. (24). In the simulation where $Cn(L) = 1$, we have $Y_0 \leqslant L$; hence the conduction along the spanwise direction affects the temperature profile located at Y_0. In other simulations ($Cn = 10, 100$) we have $Y_0 \gg L$, thus conduction in the streamwise direction does not affect the thermal profile.

5.5. Conduction, forced convection and thermal radiation

The same domain dimensions, computational grid and boundary conditions as reported in Section 5.4 are adopted. Now also radiation is also simulated in the fluid medium, and a temperature difference of $\Delta T = 100K$ is imposed between the isothermal walls. The system is governed by the three non-dimensional numbers N, Bo, Cn from which the values of $\kappa, k, \bar{u}$ can be derived.

Following the analysis of the conductive-convective case (cf. Section 5.4), the convection-conduction number is set to $Cn = 100$ for all simulations. This value guarantees that the influence of the bottom thermal layer does not affect the temperature profile in most of the cases.

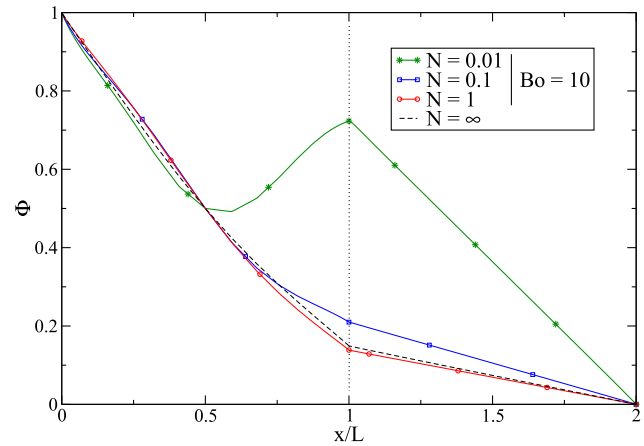

(a) Heat transfer by radiation stronger than force convection, $Bo = 10$.

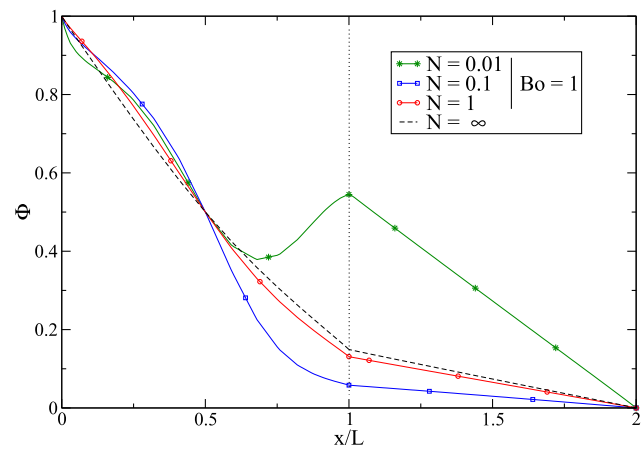

(b) Balance between radiation and force convection, $Bo = 1$.

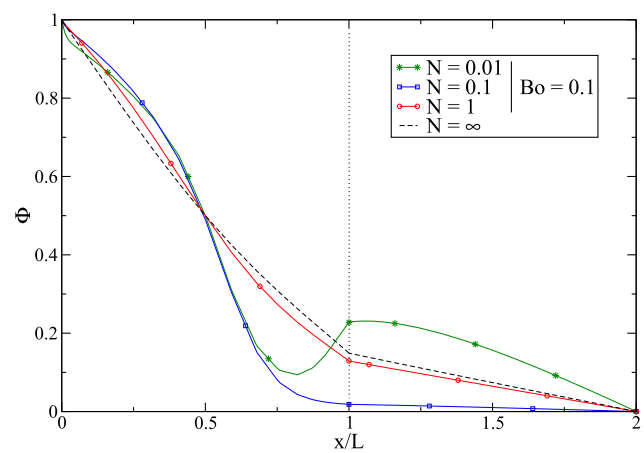

(c) Heat transfer by force convection stronger than radiation, $Bo = 0.1$.

Fig. 12. Thermal radiation, conduction and forced convection with SRHT. Non-dimensional temperature along a horizontal line $y = Y_0$ for $Cn = 100$, changing the Boltzmann number Bo and Stark number N.

Fig. 12 reports the non-dimensional temperature, see Eq. (37), profiles at the height Y_0, chosen as stated in Section 5.4. Combinations of the values $N = 1, 0.1, 0.01$ and $Bo = 10, 1, 0.1$ have been used.

Fig. 12a shows the case of high convective heat transfer compared to the radiative one ($Bo = 10$). The interface temperature, as well as the global system temperature, is higher than for lower

Bo cases. Since the high-speed flow cools down the fluid medium more effectively in the centre of the channel, Y_0 increases and the energy radiated is more effective in heating the fluid medium near the solid boundaries. The profile for $N = 0.1$ practically collapses with the one for $N = 1$ in fluid medium far from the interface, but it increases near the interface and remains higher in the solid medium. The temperature for $N = 0.01$ has a typical parabolic profile: the minimum is reached in the channel centre zone, and it is due to the convection of cold fluid medium.

Fig. 12b depicts the case of balance between convective and radiative heat transfer ($Bo = 1$). Surprisingly, the interface temperature for $N = 0.1$ is lower than for $N = 1$, even if in the former case the level of radiation is higher than in the latter. This is due to the fact that fluid conduction tends to decrease the interface temperature and thermal radiation generates a temperature sink in the near-interface zone. On the contrary, in the near-wall zone radiation contributes to increase the fluid temperature. The result is a non-monotonic thermal profile in the fluid medium. The channel is divided into two parts:

the near-wall zone ($0 \leqslant x/L \leqslant 0.5$) is influenced by emission from the isothermal hot wall. The thermal profile is concave and higher than in the $N = \infty$ case;

the near-interface zone ($0.5 \leqslant x/L \leqslant 1$) is subject to absorption of radiation by the solid interface. The thermal profile is convex and the temperature is lower than in the case of no radiation.

Graphically, the two zones are separated by an inflection point of the temperature function $T(x/L)$. The asymmetry of the profile is ascribed to the non-linearity of the radiative process (cf. Fig. 10b). The profile for $N = 0.01$ exhibits the parabolic shape already described in the previous case. However, near the isothermal wall it presents first a reduction, then an increase of temperature.

Fig. 12c reports the simulations with low level of convective heat transfer compared to the radiative one ($Bo = 0.1$). Since the convection is weak, Y_0 is very close to the bottom boundary. The effects of the isothermal fluid bottom condition on the solid temperature can be detected in the $N = 0.01$ plot: the temperature profile in the solid media is not linear but slightly convex. Also $N = 0.1$ presents a very low temperature near the interface, probably due to the thermal conduction from the bottom.

For all the *Bo* values, the low-radiation thermal profiles ($N = 1$) are similar to the one of no radiation ($N = \infty$), as expected. However, the weak effect of radiation can be detected: the temperature profiles have a slight non-monotonic behaviour, similar to the one described for the case $Bo = 1, N = 0.1$. Comparing the profiles characterised by $N = 0.01$, we can notice that the temperature minimum moves towards the isothermal wall as *Bo* increases. This effect is related to the increase of the interface temperature.

5.6. Conduction, natural convection and thermal radiation

The interaction of natural convection with radiation and conduction is studied for a cavity in contact with a conductive wall. The geometry is depicted in Fig. 9: the domain is composed by a fluid and a solid square region, with one side in common. The dimensions of the two regions are $L \times H = 1\ \text{m} \times 1\ \text{m}$. Both regions are discretised by equidistant grid of 80×80 points. After some tests, this grid it is found to be fine enough to capture the thermal boundary layer. The domain is bounded by two isothermal walls (hot at the left, cold at the right), and two horizontal insulator walls (top and bottom). The temperature difference between the isothermal walls is set to $\Delta T = 1000$ K. In the fluid region a natural convection arises and the buoyancy force drives the fluid medium. The no-slip condition is applied at the walls.

Three cases are simulated for different degrees of radiation $N = 1, 0.1, 0.01$ and $Cn = 100, Bo = 1$. The characteristic buoyant velocity

$$U = \sqrt{(g\beta_T \Delta T L)}, \tag{41}$$

is used for computing the non-dimensional numbers. The gravity acceleration is $g = 9.81\ \text{m/s}^2$ and the value of thermal expansion coefficient β_T is changed in the three simulations. The fluid dynamic viscosity ν is chosen in a way that

$$Re = \frac{UL}{\nu} = \sqrt{\frac{g\beta_T \Delta T L^3}{\nu^2}} = 100, \tag{42}$$

where *Re* is the Reynolds number, *i.e.* the ratio between the inertial forces and the viscous forces. Such a constrain guarantees a laminar flow in all simulations. The resulting flow is a clockwise circular motion, not perfectly symmetric because of the non-homogeneous temperature profile arising at the interface, see Fig. 14.

Fig. 13 visualises the temperature distributions for the three values of the Stark number. Fig. 13a shows the case of high degree of thermal radiation. The system is dominated by radiation, that

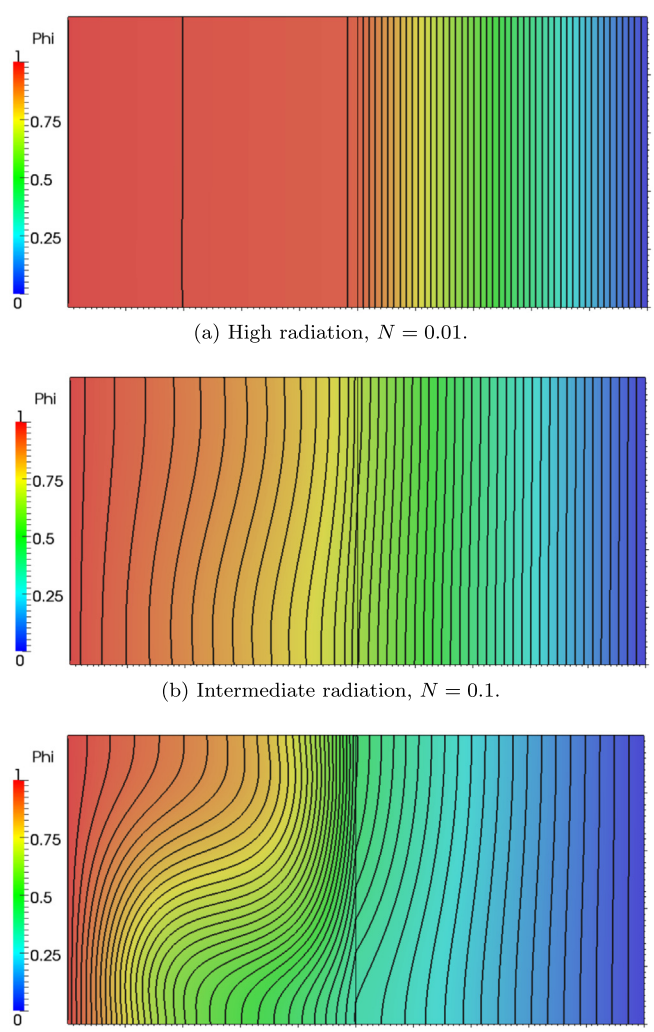

(a) High radiation, $N = 0.01$.

(b) Intermediate radiation, $N = 0.1$.

(c) Low radiation, $N = 1$.

Fig. 13. Temperature contour plots in fluid and solid medium for three level of radiation, $Bo = 1, Cn = 100$. Contour line values: 50 values over an equispaced partition of temperature range.

heats up the fluid medium until it reaches almost the same temperature as the isothermal wall. The contour lines are practically vertical since the flow field, generated by the low fluid thermal gradient, is so weak that it cannot significantly alter the thermal distribution. Fig. 13b depicts the case of balance between radiation and conduction. A more uniform temperature distribution arises in both the fluid and solid regions. The natural convection changes the thermal distribution in the fluid medium but also in the solid medium, near the interface. Fig. 13c presents the cases of low radiation and high conduction. In this case, radiation cannot stabilise the interface temperature and the convective flow leads to hot top and cold bottom zones, respectively, in the fluid medium. Also the solid medium temperature is significantly influenced by the fluid convection.

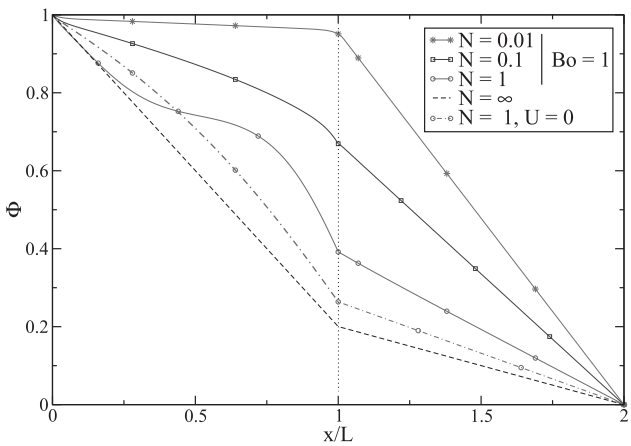

(a) Non-dimensional temperature for different N. Case of low radiation ($N = 1$) and no convection ($U = 0$) is reported (red dash line).

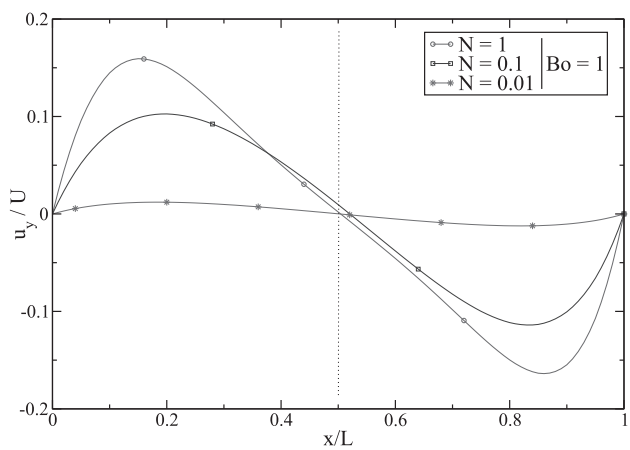

(b) Vertical components of non-dimensional velocity u_y/U over a horizontal line $y/H = 0.5$ in fluid medium.

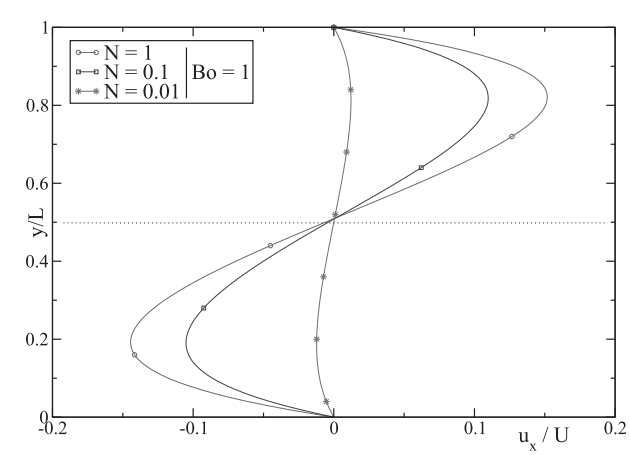

(c) Horizontal components of non-dimensional velocity u_x/U over a vertical line $x/L = 0.5$ in fluid medium.

Fig. 14. Thermal radiation, conduction and natural convection with SRHT. Non-dimensional temperature and velocity profiles in fluid medium. Different values of Stark number N and $Bo = 1, Cn = 100$.

The non-dimensional temperature and velocity profiles for the aforementioned cases are reported in Fig. 14, along vertical and horizontal lines passing through the fluid region centre. Fig. 14a shows the non-dimensional temperature profiles, see Eq. (37), across the fluid and solid media. It can be pointed out that this is not directly comparable with Fig. 10b of the previous section, since the optical thickness τ_L of the two sets of simulations is not the same. However, the thermal profiles share the same qualitative behaviour, except for the case of low radiation $N = 1$. In accordance with Fig. 13b, the natural convective flow increases the temperature near the interface and decreases it near the isothermal wall. The profile for the same case, where natural convection is not activated, is also reported (labelled $N = 1, U = 0$) for comparison. The interface temperature is significantly increased by the fluid flow. In the other cases, the profiles obtained with and without convection are practically the same, thus they are not reported. Fig. 14b presents the non-dimensional vertical fluid velocity along a horizontal line ($y/H = 0.5$); and Fig. 14c reports the non-dimensional horizontal velocity along a vertical line ($x/L = 0.5$). When thermal radiation increases the temperature, the gradient in fluid medium decreases, leading to a weaker buoyancy force and, eventually, a lower velocity field. The system is not perfectly symmetric because of the non-uniform temperature at the interface. The velocity asymmetry is more evident for the case $N = 0.1$, and less for the case $N = 1$, while it is almost negligible for $N = 0.001$ (as expected after the analyses of the interface temperature in contour plots).

6. Conclusions

A numerical solver for heat transfer problems is developed, considering CHT between solid and fluid media as well as the contemporary presence of conduction, convection and radiation. Thermal radiation is modelled through the first-order, spherical approximation method (P_1-model). A Neumann-Neumann conjugate heat transfer technique is used to simulate the heat transfer between the two media, and a numerical coupling strategy for the heat transfer modes is described. The model is used in idealised cases, for a parametric study of thermal radiation associated with conduction, convection and the fluid–solid surface heat transfer. In successive studies, the thermodynamic model herein presented can be integrated in a generic three-dimensional transient thermo-fluid dynamics solver.

In the first part, the P_1 radiative model without surface radiative heat transfer is validated. Several benchmark cases reported in the literature are successfully reproduced and the prediction capability of the model is investigated.

The numerical implementation is, then, verified using a simplified case. A comparison between the P_1 solution with the exact solution, points out the general tendency of the model to overestimate the radiative effects, as expected. However, in this case the overestimation is probably exaggerated by the unrealistic difference of temperature at the boundaries.

Radiation effects are then studied when combined with other heat transfer modes: pure radiation, radiation-conduction, radia tion-conduction–convection. Two archetypal geometries are investigated: two infinitely long parallel plates and a square cavity. An

excellent agreement with the reference solutions is achieved for a two parallel plates case. In square cavity case, the results are less accurate for optical thick medium and near the square corners, where collimated irradiation occurs. These are two well known limits of the P_1-model (Ref. [23]). Moreover, the model fails in reproducing a pure scattering medium because in this particular case the governing equation reduces to a Laplace equation. Thus, radiation is completely determined by the Marshak's boundary condition, that is recognised to be not accurate [20] and tends to overestimate the emitted radiation. Conversely, when a participating medium is present, the effects of boundary emission are reduced and, overall, better results are achieved. Overall, the P_1-model gives satisfactory results, despite the simplicity of the mathematical model. It appears to be more trustworthy when associated with other heat transfer mechanisms and less idealised case settings.

Summing up, the main prediction limits of the P_1-model are:

1. tendency to overestimate the RHT effects;
2. loss of accuracy in case of collimated radiation;
3. incorrect results for low participating media, because of Marshak's boundary condition influence;
4. imprecise for optical thick medium ($\tau \gg 1$).

Although the aforementioned limitations, the P_1-approximation requires a lower computational cost if compared to more accurate methods, like DOM. This is essential in transient simulations, where temperature-radiation and fluid–solid thermal coupling loops have to be performed in order to ensure the instantaneous thermal equilibrium.

In the second part, the influence of surface radiative heat transfer is studied in new benchmark case: a fluid medium in contact with a solid one, both bounded by isothermal walls. Different simulations are performed in order to investigate the interaction of surface radiative heat transfer with: (i) radiation-conduction, (ii) radiation-conduction-force convection, (iii) radiation-conduction-natural convection. The non-dimensional numbers characterising the mutual influence of the heat transfer modes are derived and adopted for a parametric investigation. Overall, the results are in accordance with the physics of thermal radiation. The simulation of conjugate heat transfer points out that thermal interaction between fluid and solid media strongly affects the thermodynamics of the systems. Thermal radiation intensifies such interaction, increasing the interface temperature and developing non-linear temperature profile in the fluid medium. In case (i), the heat fluxes ratio number H_f is introduced and used to identify the conductive boundary layer near the solid walls, and the effects of different wall emissivity is also studied. In case (ii), the heat transfer is investigated in a laminar channel flow with cold inflow. Radiation is particularly effective in transporting energy through the channel and increasing the interface temperature, even if the fluid has a lower temperature. The convective-conductive number is used to analysed the influence of the cold inflow along the streamwise direction. In case (iii), the presence of radiation decreases the buoyancy force by reducing the thermal gradient, while the conjugate heat transfer makes the system asymmetric. From a numerical side, the coupling strategy appears to be stable in all the cases simulated.

Acknowledgements

This work was supported by Regione Friuli-Venezia Giulia – DITENAVE – Progetto "CFD OPEN SOURCE PER OPERA MORTA-COSMO" n. CUP J94C14000090006.

References

[1] P. Asinari, S.C. Mishra, R. Borchiellini, A lattice boltzmann formulation to the analysis of radiative heat transfer problems in a participating medium, Numer. Heat Transfer, Part B. Fundam. 52 (2010) 126.
[2] D.G. Barhaghi, L. Davidson, Large-eddy simulation of mixed convection-radiation heat transfer in a vertical channel, Int. J. Heat Mass Transfer 52 (2009) 3918.
[3] M.G. Carvalho, T.L. Farias, Modelling of heat transfer on radiation and conbusting systems, Chem. Eng. Res. Des. 76 (1998) 175.
[4] X. Cheng, U. Müller, Turbulent natural convection coupled with thermal radiation in large vertical channels with asymmetric heating, Int. J. Heat Mass Transfer 12 (1998) 1692.
[5] C. Cintolesi, Large-eddy Simulations of Conjugate Heat Transfer with Evaporation-condensation and Thermal Radiation Ph.D. thesis, University of Trieste, School of Environmental and Industrial Fluid Mechanics, 2016, 29 April NBN: to be assigned.
[6] C. Cintolesi, A. Petronio, V. Armenio, Large eddy simulation of turbulent buoyant flow in a confined cavity with conjugate heat transfer, Phys. Fluids 27 (2015).
[7] A.L. Crosbie, P. Schrenker, Radiative transfer in a two-dimensional rectangular medium exposed to diffuse radiation, J. Quant. Spectrosc. Radiat. Transfer 31 (1984) 339.
[8] A. Dorfman, Z. Renner, Conjugate problems in convective heat transfer: review, Math. Prob. Eng. 2009 (2009).
[9] F. Duchaine, A. Corpron, L. Pons, V. Moureau, F. Nicoud, T. Poinsot, Development and assessment of a coupled strategy for conjugate heat transfer with large eddy simulation: application to a cooled turbine blade, Int. J. Heat Fluid Flow 30 (2009) 1129.
[10] F. Duchaine, S. Mendez, F. Nicoud, A. Corpron, V. Moureau, T. Poinsot, Conjugate heat transfer with large eddy simulation for gas turbine components, C. R. Mec. 337 (2009) 550.
[11] A. Fedorov, R. Viskanta, Turbulent natural convection heat transfer in an asymmetrically heated, vertical parallel-plate channel, Int. J. Heat Mass Transfer 40 (1997) 3849.
[12] T. Fusegi, B. Farouk, Laminar and turbulent natural convection-radiation interaction in a square enclosure filled with a nongray gas, Numer. Heat Transfer, Part A. Appl. 15 (1989) 303.
[13] A. Garai, J. Kleissl, S. Sarkar, Flow and heat transfer in convectively unstable turbulent channel flow with solid-wall heat conduction, J. Fluid Mech. 757 (2014) 57.
[14] P. Hassanzadeh, G.D. Raithby, Efficient calculation of radiation heat transfer in participating media, J. Thermophys. Heat Transfer 22 (2008) 129.
[15] H.C. Hottel, A.F. Sarofim, Radiative Transfer, first ed., McGraw-Hill Book Company, 1967.
[16] J.R. Howell, The monte carlo method in radiative heat transfer, J. Heat Transfer 120 (1997) 547.
[17] J.R. Howell, M.P. Mengüç, R. Siegel, Thermal Radiation Heat Transfer, sixth ed., Taylor and Francis – CRC Press, 2015.
[18] J.R. Howell, R. Siegel, M.P. Mengüç, Thermal Radiation Heat Transfer, fifth ed., Taylor and Francis, 2011.
[19] K. Lari, M. Baneshi, S. Gandjalikhan Nassab, A. Komiya, S. Maruyama, Combined heat transfer of radiation and natural convection in a square cavity containing participating gases, Int. J. Heat Mass Transfer 54 (2011) 5087.
[20] F. Liu, J. Swithenbank, E.S. Garbett, The boundary condition of the p_n-approximation used to solve the radiative transfer equation, Int. J. Heat Mass Transfer 35 (1992) 2043.
[21] S.C. Mishra, H. Poonia, A.K. Das, P. Asinari, R. Borchiellini, Analysis of conduction-radiation heat transfer in a 2d enclosure using the lattice boltzmann method, Numer. Heat Transfer, Part A. Appl. 66 (2014) 669.
[22] M.F. Modest, Radiative equilibrium in a rectangular enclosure bounded by gray walls, J. Quant. Spectrosc. Radiat. Transfer 15 (1975) 339.
[23] M.F. Modest, Radiative Heat Transfer, third ed., Elsevier, 2013.
[24] F. Moufekkir, M. Moussaoui, A. Mezrhab, H. Naji, D. Lemonnier, Numerical prediction of heat transfer by natural convection and radiation in an enclosure filled with an isotropic scattering medium, J. Quant. Spectrosc. Radiat. Transfer 113 (2012) 1689.
[25] M.M. Razzaque, D.E. Klein, J.R. Howell, Finite element solution of radiative heat transfer in a two-dimensional rectangular enclosure with gray participating media, ASME J. Heat Transfer 105 (1983) 933.
[26] M.M. Razzaque, D.E. Klein, J.R. Howell, Coupled radiative and conductive heat transfer in a two-dimensional rectangular enclosure with gray participating media using finite elements, ASME J. Heat Transfer 106 (1984) 613.
[27] D.R. Rousse, Numerical predictions of two-dimensional conduction, convection, and radiation heat transfer. i. formulation, Int. J. Therm. Sci. 315 (2000) 97.
[28] D.R. Rousse, G. Gautier, J.F. Sacadura, Numerical predictions of two-dimensional conduction, convection, and radiation heat transfer. ii. validation, Int. J. Therm. Sci. 332 (2000) 97.
[29] P. Sosnowski, Numerical Investigation of Evaporation and Condensation of Thin Films in Conjugated Heat Transfer Systems Ph.D. thesis, School of Environmental and Industrial Fluid Mechanics, University of Trieste, 2013, NBN urn:nbn:it:units-10080.

[30] P. Sosnowski, A. Petronio, V. Armenio, Numerical model for thin liquid film with evaporation and condensation on solid surfaces in a systems with conjugated heat transfer, Int. J. Heat Mass Transfer 66 (2013) 382.
[31] E. Sparrow, S. Shah, C. Prakash, Natural convection in a vertical channel: I. Interacting convection and radiation. ii. The vertical plate with and without shrouding, Numer. Heat Transfer 3 (1980) 297.
[32] I. Tiselj, R. Bergant, B. Mavko, I. Bajsić, G. Hetsroni, Dns of turbulent heat transfer in channel flow with heat conduction in the solid wall, J. Heat Transfer 123 (2001) 849.
[33] S. Venkateshan, K.K. Prasad, Radiative interactions in boundary layers, J. Fluid Mech. 90 (1979) 33.
[34] R. Viskanta, Interaction of heat transfer by conduction, convection, and radiation in a radiating fluid, ASME J. 85 (1963) 318.
[35] R. Viskanta, Radiative Transfer in Combustion systems: Fundamental and Applications, Begell House Publishers, 2005.
[36] R. Viskanta, Computation of radiative transfer in combustion systems, Int. J. Numer. Method Heat Fluid Flow 18 (2008) 415.
[37] R. Viskanta, M.P. Mengüç, Radiation heat transfer in combustion systems, Prog. Energy Combust. Sci. 13 (1987) 97.
[38] J. Wang, J. Li, J. Jackson, A study of the influence of buoyancy on turbulent flow in a vertical plane passage, Int. J. Heat Fluid Flow 25 (2004) 420.
[39] J. Xamna, J. Arcea, G. Ivareza, Y. Chveza, Laminar and turbulent natural convection combined with surface thermal radiation in a square cavity with a glass wall, Int. J. Therm. Sci. 47 (2008) 1630.
[40] S. Xin, J. Salat, P. Joubert, A. Sergent, F. Penot, P. Le Quéré, Resolving the stratification discrepancy of turbulent natural convection in differentially heated air-filled cavities - part III: A full convectionconductionsurface radiation coupling, Int. J. Heat Fluid Flow 42 (2013) 33.